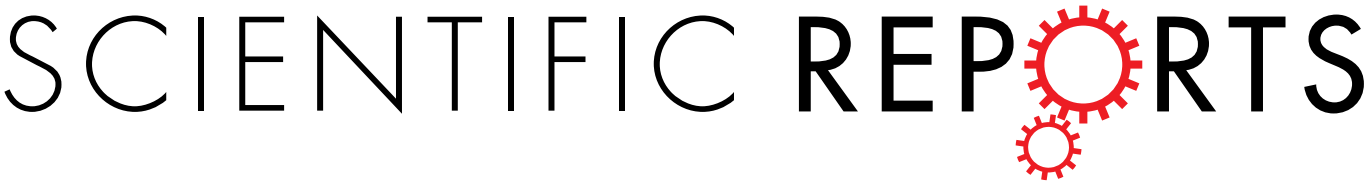

OPEN

New insights towards strikingly improved room temperature ethanol sensing properties of p-type Ce-doped SnO_2 sensors

Received: 15 December 2017
Accepted: 8 May 2018
Published online: 24 May 2018

Manjeet Kumar[1], Vishwa Bhatt[1], A. C. Abhyankar[2], Joondong Kim[1], Akshay Kumar[3], Sagar H. Patil[4] & Ju-Hyung Yun[1]

In this article, room temperature ethanol sensing behavior of p-type Ce doped SnO_2 nanostructures are investigated successfully. Interestingly, it is examined that the abnormal n to p-type transition behavior is caused by Ce doping in SnO_2 lattice. In p-type Ce doped SnO_2, Ce ion substituting the Sn is in favor of generating excess holes as oxygen vacancies, which is associated with the improved sensing performance. Although, p-type SnO_2 is one of the important materials for practical applications, it is less studied as compared to n-type SnO_2. Pure and Ce doped SnO_2 nanostructures were successfully synthesized by chemical co-precipitation method. The structure, surface morphology, unpaired electrons (such as free radicals), and chemical composition of obtained nanoparticles were studied by various kinds of characterization techniques. The 9% Ce doped SnO_2 sensors exhibit maximum sensor response of ~382 for 400 ppm of ethanol exposure with fast response time of ~5 to 25 sec respectively. Moreover, it is quite interesting that such enhancement of ethanol sensing is unveiled at room temperature, which plays a key role in the quest for better ethanol sensors. These remarkably improved sensing results are attributed to uniformly distributed nanoparticles, lattice strain, complex defect chemistry and presence of large number of unpaired electrons on the surface.

In past six decades, metal oxide semiconductors (MOS) have been one of the most prevailing gas sensing materials among large miscellany of materials on the grounds of its low production cost, tranquility during use and prominent selectivity for various gases in addition to high detection[1–5]. Over the past few decades, an intense requirement of gas sensors has become progressively greater by virtue of elevated atmospheric pollution leading towards the emission of hazardous gases[6–10]. One of the vital requirements of such gas sensors can be ethanol sensors. Those working on ethanol synthesis, experience hardship from the huge probability of being victims of digestive track cancer and increased risk of respiratory symptoms of a threshold limit (1000 ppm). Thus, an increasing demands and emerging challenges for detection of ethanol gas at ppm/ppb level have enforced the researchers to fabricate low cost, high performance and relatively stable ethanol sensors. With the growing interest in progression of sensing devices, more and more exhilarating results of MOS have been reported in literature[10–14]. The gas sensors developed by various types of MOS exhibited good sensitivity to ethanol at different operating temperatures (OT)[15–19] suggesting that most of the ethanol sensors work at higher temperature. Various MOS such as TiO_2, GeO_2, Cr_2O_3, Mn_2O_3, NiO, CuO, CdO, CeO_2, MgO, BaO, In_2O_3, WO_3, V_2O_3, Fe_2O_3, Nb_2O_5, MoO_3, Co_3O_4, Ta_2O_5, La_2O_3, Nd_2O_3 etc. are well-known and widely used for metal oxide based sensors for the detection of different chemical inputs[20,21].

Among them, pure SnO_2 is one of the most prominent n-type, wide band gap (3.6 eV) MOS with a carrier concentration of $5.7 \times 10^{20}\,cm^{-3}$ making it an outstanding material for chemical gas sensors[22–24]. Although pure SnO_2 has an excellent sensitivity but the major drawbacks are its poor selectivity which hinders a lot to meet

[1]Department of Electrical Engineering, Incheon National University, Incheon, 406772, South Korea. [2]Department of Materials Engineering, Defence Institute of Advanced Technology, Girinagar, Pune, 411025, India. [3]Department of Nanotechnology, Sri Guru Granth Sahib World University, Fatehgarh Sahib, 140 407, Punjab, India. [4]Center for material characterization, CSIR-National chemical laboratory, Pashan, Pune, 411008, India. Correspondence and requests for materials should be addressed to A.C.A. (email: ashutoshabhyankar@gmail.com) or J.-H.Y. (email: juhyungyun@inu.ac.kr)

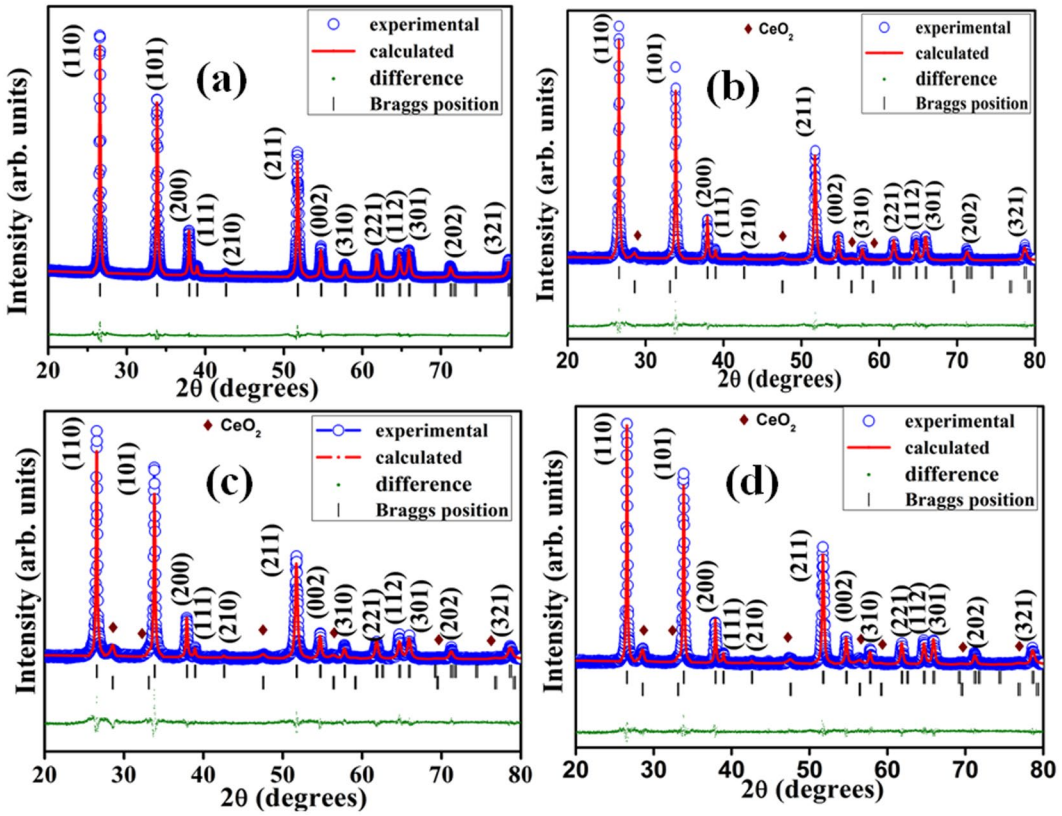

Figure 1. Rietveld fit of pure SnO_2 and Ce doped SnO_2 nanomaterial with addition of different concentrations of Ce: (**a**) 0%, (**b**) 3%, (**c**) 6% and (**d**) 9%.

up all practical key parameters such as high sensitivity, faster response-recovery time, stability and low power consumption for realistic sensor applications[20,25–28]. Thus, despite of substantial research work carried out on sensing materials, still there is a scope of exploration to achieve higher sensitivity and better selectivity for hazardous gases at room temperature (RT). For that, metal ion doping in SnO_2 lattice may be one of the influencing factors for the furtherance in sensing properties of SnO_2[29]. In case of doped SnO_2, substitutional and interstitial point defects may exist depending on the rearrangement of the internal defects in SnO_2 lattice[30]. In addition, the semiconducting behavior can be predicted depending on the type of doping (donor or acceptor) introduced to the host material in order to tailor the band bending and band alignments on which the amount of gas sensing enhancement relies. It is noteworthy that gas sensing has been explored using SnO_2 exhibiting n-type behavior but their equivalent p-type counterpart was unexpectedly absent for a long time. In past a decade, the exploration of novel p-type SnO_2 for gas sensors has been started[31–33] and the researchers and technologists around the globe are making an effort to discover an effective method to attain the p-type conduction in the n-type SnO_2. In literature, p-type conductivity in SnO_2 has been achieved by doping M_{Sn} metal ions (where, M = Li, Al, Ga, In and Cd) acting as a substitutional dopant in SnO_2 playing an important role to enhance the gas sensing characteristics[30,34,35]. Hence, the understanding of synthesis and fabrication of p-type SnO_2 gas sensors would be a worthy research area to open up several new possibilities in device applications.

In this study, authors have used the state of art to explore p-type conduction mechanism in Ce-doped SnO_2 to characterize RT ethanol sensing. Although Ce-doped n-type SnO_2 based sensors have already been used for the detection of ethanol but reported operating temperatures of these sensors are as high as 300 to 500 °C[21,27,36] and no reports have been shown on p-type conduction in Ce-doped SnO_2 ethanol sensors at RT. Therefore, the fabrication of stable and highly selective gas sensing materials working at RT is still highly desirable. Present work demonstrated the RT ethanol sensors based on p-type Ce-doped SnO_2 nanostructured devices to understand their mechanism under consideration of several aspects that influence the sensor performance including defect chemistry, surface morphology, several diffusion processes, and associated unpaired electrons in the form of free radicals. However, from the literature and present study, authors realized that the level of understanding of these mechanisms is still lacking and in-depth research in this area is required. To the best of our knowledge, it is the first systematic report on p-type Ce doped SnO_2 nanostructure based RT ethanol sensor. The results described in this article indicates that 9 wt % Ce doped SnO_2 sensor is highly sensitive and selective towards ethanol detection at RT.

Results

XRD analysis. The XRD patterns of pure and Ce doped SnO_2 nanostructured samples are elucidated in Fig. 1. As it can be seen that, pure SnO_2 have tetragonal rutile structure which is indexed with JCPDS file 00-041-1445[37].

Samples wt.% of Ce	Atomic position	x	y	z	Phase Fraction (%)		χ^2	Lattice Parameter		Volume (Å)^3	Strain
								a (Å)	*c* (Å)		
0	Sn	0.00	0.00	0.00	SnO_2	100	1.96	4.741	3.188	71.656	1.28×10^{-3}
	O	0.301	0.301	0.00							
3	Sn	0.00	0.00	0.00	SnO_2	93.23	1.70	4.742	3.189	71.709	2.3×10^{-3}
	O	0.30	0.30	0.00	CeO_2	6.77					
6	Sn	0.00	0.00	0.00	SnO_2	90.68	2.08	4.743	3.190	71.762	3.2×10^{-3}
	O	0.299	0.299	0.00	CeO_2	9.32					
9	Sn	0.00	0.00	0.00	SnO_2	85.85	2.3	4.744	3.191	71.815	3.4×10^{-3}
	O	0.298	0.298	0.00	CeO_2	14.15					

Table 1. Atomic position, Phase fraction, Lattice parameter, Volume, χ^2 values obtained by Rietveld refinement and strain value using W-H analysis.

It has been observed from Fig. 1(b–d) that Ce doped SnO_2 nanostructured samples have all the peaks of SnO_2 with a few peaks of CeO_2. These peaks were indexed with the JCPDS files of SnO_2 and CeO_2 (JCPDS file no.: 01-075-0120)[38]. The XRD pattern of pure and Ce doped SnO_2 nanomaterials have been refined by Rietveld refinement using FULLPROF Suite programme. The background for all samples was refined by 6th degree Polynomial function. The pseudo-voigt profile function (linear combination of Gaussian and Lorentzian) was used to describe the peak shape of all the samples. The Rietveld refinement data of pure and Ce doped SnO_2 nanomaterial samples are summarized in Table 1. It can be seen from Fig. 1 that the diffraction peaks of all the samples were well fitted. The lattice parameters, atomic position and phase fraction are listed in Table 1. The increase in magnitude of lattice parameter and cell volume of Ce doped SnO_2 are shown in Table 1. The lattice parameter 'a' and 'c' of the Ce doped SnO_2 unit cell is found to increase linearly with the Ce concentration following Vegards law[39,40] which is shown in figure (see Supporting Information, Fig. S1). It is also observed that the full width at half maxima (FWHM) increases with an increase in Ce content in the SnO_2. Hence, this indicates that Ce doping in the SnO_2 lattice leads to decrease in crystallite size. From the increased lattice constant with the addition of Ce content, it is confirmed that Ce ions have been effectively doped in SnO_2 lattice and some part is present in the form of CeO_2[36,41]. The substitution of Sn by Ce creates vacancies and disturb local arrangements of the crystal structure which is further confirmed from ESR analysis. Similar observations have been reported in the literature by Yang *et al.*[42]. The slight deviation in atomic position has been observed that may induce lattice strain which is further confirmed from the Williamson-Hall plot[43] (see Supporting Information, Fig. S2). The value of average micro-strain for pure SnO_2 is 1.28×10^{-3} and found to be increased in case of 9% Ce doped SnO_2 nanomaterial which is shown in Table 1. It shows that with the increased Ce content in SnO_2, the little deviation in atomic position is found and lattice constant also increases with an increase in micro strain values from 1.28×10^{-3} to 3.4×10^{-3}. Due to incorporation of Ce ions into the SnO_2 lattice, this causes increase in lattice parameter and micro strain. The influences of increased lattice parameter and micro strain on sensing characteristics have been discussed at the end of this section. The surface morphology and elemental composition of the sensor materials have been studied using FESEM and EDS measurement (see Supporting Information, Figs S3 and S4).

TEM and HRTEM analysis. Figure 2(a–c) shows the TEM images of pure and Ce doped SnO_2 nanomaterials. From TEM images, it is clear that the particle size is decreasing with the addition of Ce content. The nanoparticles are random/polygon in shape with the average particle size of ~16 nm, ~12 nm and ~6 nm for Pure SnO_2, and Ce doped SnO_2 (0, 6 and 9%) respectively. 9% Ce doped SnO_2 nanomaterial results in formation of uniformly distributed nanoparticles of approximately ~6 nm particle size, which is twice of the Debye length for SnO_2. The Fig. 3(a,b) shows the HRTEM images of pure and Ce doped SnO_2 nanomaterials where we can clearly see the lattice resolution of individual nanoparticles. The distance between the lattice planes for pure SnO_2 is found to be 0.33 nm which is associated to the (110) plane of tetragonal SnO_2. The marked lattice fringes of 9% Ce doped SnO_2 sample is found to be 0.35 nm and 0.25 nm corresponding to (110) and (101) planes of tetragonal SnO_2 respectively. The selected area diffraction (SAD) patterns recorded for pure and Ce doped SnO_2 nanomaterials are shown in Fig. 3(c,d) which clearly reveal the polycrystalline nature of pure and Ce doped SnO_2. The diffraction rings of pure SnO_2 are indexed as (110), (101), (200), (211) and (301) confirming the tetragonal rutile structure. SAD pattern acquired for 9% Ce doped SnO_2 also confirms the formation of tetragonal rutile structure. These results are consistent with the above mentioned XRD results.

ESR analysis. The presence of unpaired electrons in the form of free radicals and charge carriers has been studied using ESR spectroscopy. The Fig. 4 shows the ESR dispersion derivative (dp/dH) as a function of magnetic field. The ESR measurements were performed at microwave frequency of ~9.45 GHz (X-band). When the external magnetic field is applied, the spin interactions of the unpaired electrons can be studied from ESR spectra recorded for pure and Ce doped SnO_2 at RT. As it is known that the spin quantum number (s) of ½ with the magnetic moments consisting of two magnetic components ms = +½ and −½ in parallel and antiparallel respectively. These magnetic components are aligned to the applied field with the strength of B_o having a specific energy. There is a possibility of either absorption or emission of electromagnetic radiation by unpaired electrons and they also consist of two energy levels between which the unpaired electrons can move. The change in the two energy levels of an electron can be obtained by $\Delta E = g\mu_B B_0$, where, g and μ_B are electron's g factor and Bohr magnetron

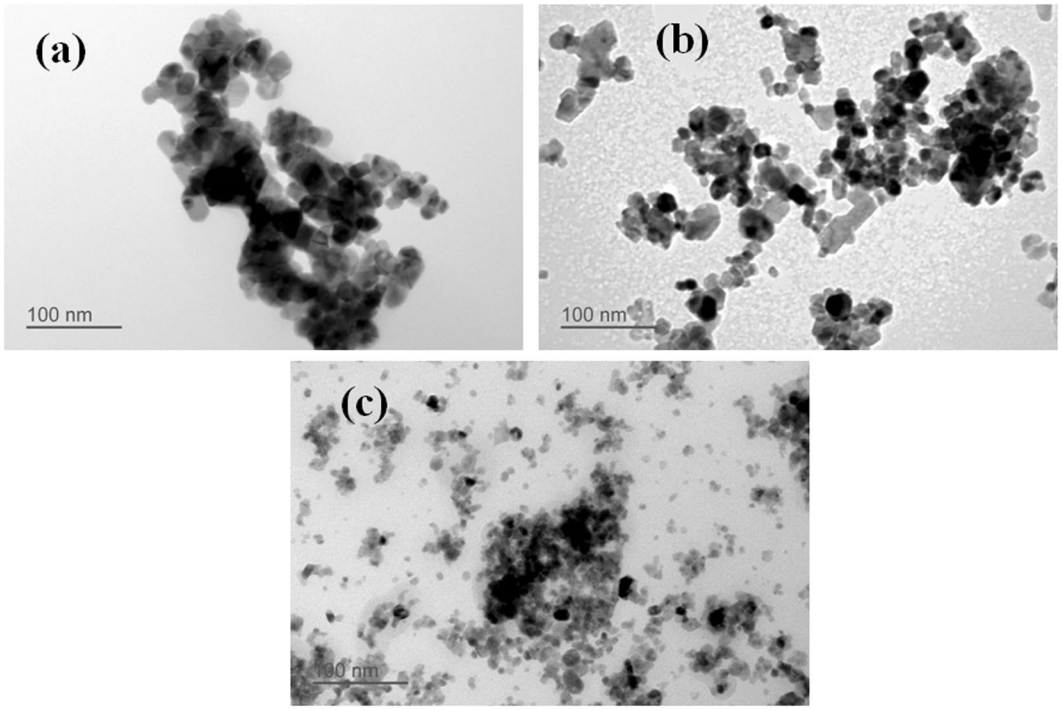

Figure 2. TEM micrograph of pure and Ce doped SnO_2 with addition of different concentrations of Ce: (**a**) 0%, (**b**) 6% and (**c**) 9%.

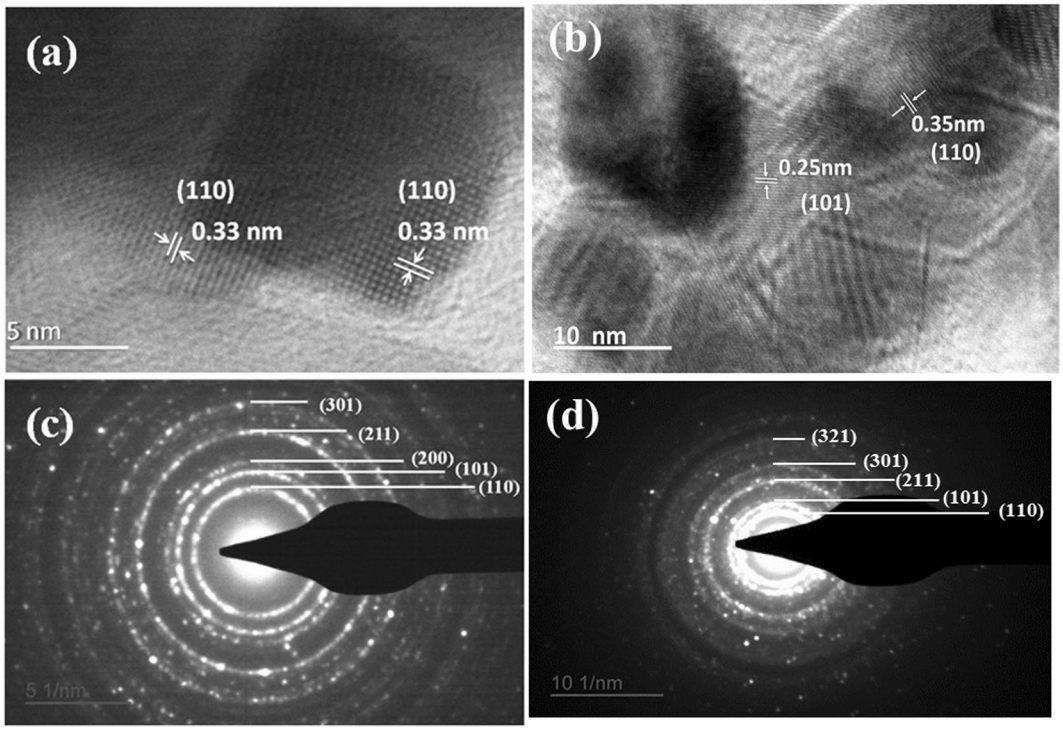

Figure 3. HRTEM micrograph of (**a**) pure SnO_2 (**b**) 9% Ce doped SnO_2 samples. SAD pattern of the (**c**) pure SnO_2 (**d**) 9% Ce doped SnO_2 samples.

($\mu_B = 9.274 \times 10^{-24} JT^{-1}$) respectively. ESR spectra show a resonance at 336.07, 336.1, 336.2 and 336.4 mT for pure and Ce doped SnO_2 (0, 3, 6 and 9%) samples respectively. Although resonance field is not affected much, Fig. 4 shows that peak to peak line width and power absorption during resonance increases remarkably upon Ce addition. Small ΔHpp and high intensity observed in 9% Ce doped SnO_2 may be attributed to the existence of large number of intrinsic oxygen vacancies. The g-value for all samples were calculated from resonance magnetic field

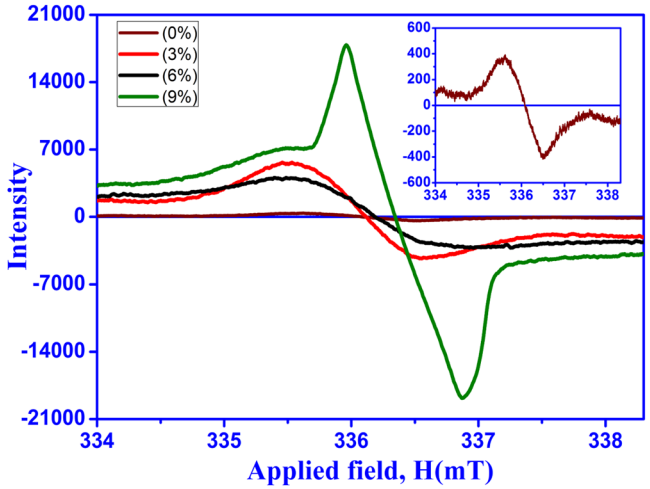

Figure 4. ESR spectra of pure and Ce doped SnO_2 with addition of different concentrations of Ce: (**a**) 0%, (**b**) 3%, (**c**) 6% and (**d**) 9%. Inset shows the ESR spectra of pure SnO_2.

Samples	g-factor	ΔH_{pp} (mT)
Pure SnO_2	2.009	1.32
3 wt.% Ce doped SnO_2	2.009	1.26
6 wt.% Ce doped SnO_2	2.007	1.46
9 wt.% Ce doped SnO_2	2.008	0.92

Table 2. ESR data of pure and Ce doped SnO_2 samples.

as shown in Table 2, which is nearly equal to the g–value of (2.008) of free electron[44]. The g-factor was calculated as $g = h\vartheta/\mu_B B_0$ similar to the reported in literature[45]. The width of the ESR signal was found to be the lowest (~0.92) in 9% Ce doped SnO_2 sample. The narrowing of ESR line is attributed to strong exchange of unpaired electrons and delocalization of unpaired electrons over a large system of conjugated chemical bonds[46]. Thus, the defect chemistry of Ce-doped samples were characterized by studying the presence of free electrons using ESR spectroscopy and the analysis suggested that Ce doping in SnO_2 create a huge amount of free electrons which is certainly responsible for improved sensitivity.

XPS analysis. The core level x-ray photoelectron spectra's of 9 wt.% Ce doped SnO_2 sample has been investigated in vacuum of the order of 2.4×10^{-9} torr. All obtained peaks were fitted by the coalition of Lorentzian and Gaussian function to reduce the least square error of the fit. A linear and tougaard background function was used to account the inelastic background in the XPS spectrum. All the XPS spectra shown in Fig. 5, are referenced to C 1 s peak (284.6 eV). The deconvoluted XPS core level Sn 3d spectra's of 9 wt.% Ce doped SnO_2 sample indicates the presence of Sn with two oxidation state i.e Sn^{2+} and Sn^{4+} respectively shown in Fig. 5(a)[47–50]. Figure 5(b) shows the deconvoluted XPS core level Ce 3d spectra of 9 wt.% Ce doped SnO_2 sample. The valence state of Ce 3d was determined by deconvolation of Ce 3d spectra. The Ce 3d spectra is fitted with the five subpeaks. These subpeaks corresponding to Ce^{3+} and Ce^{4+} valance state respectively. In Fig. 5(b), binding energy at 882.2 eV, 900.8 eV and 916.7 eV sub peaks were assigned to Ce^{4+} valance state[51–53], whereas 885.8 eV and 903.9 eV sub peaks were attributed to Ce^{3+} valence state[54,55]. Above results confirmed that 9 wt.% Ce doped SnO_2 sample displayed the presence of mixed valence state of Ce^{3+} and Ce^{4+} with the relative percentage of 70% and 30% respectively. This suggest that the content of Ce^{3+} is higher than Ce^{4+} valence state, which indicates that Ce^{3+} ion were substituted into SnO_2 lattice. Hence Ce^{3+} substitution at Sn^{4+} site is a firm reason for n to p-type transition by Ce doping in SnO_2 lattice which is further confirmed from Hall measurement results (see Supporting Information, Table S1). The substitution at Sn^{4+} by Ce^{3+} triggered the creation of oxygen vacancy defects in SnO_2 lattice, which is well matched with ESR results. The O 1 s spectrum for 9 wt.% Ce doped SnO_2 presented in the Fig. 5(c). It has been observed from the Fig. 5(c), that two components are present at 530.5 eV and 531.7 eV. This first peak (530.5 eV) is associated to lattice oxygen bound to Sn[56,57] and second peak at 531.7 eV corresponds to oxygen deficient region in SnO_2 matrix[58,59].

Sensing measurements. The gas sensing measurements of pure and Ce doped SnO_2 sensors were performed at RT for ethanol detection. Before starting the measurements, each sensor was initially purged with synthetic air for 10 minutes to stabilise the base line resistance. The exposure time to the chemical inputs was maintained to be 5 sec and for recovery, the exposure to reference synthetic air was maintained to 10 sec

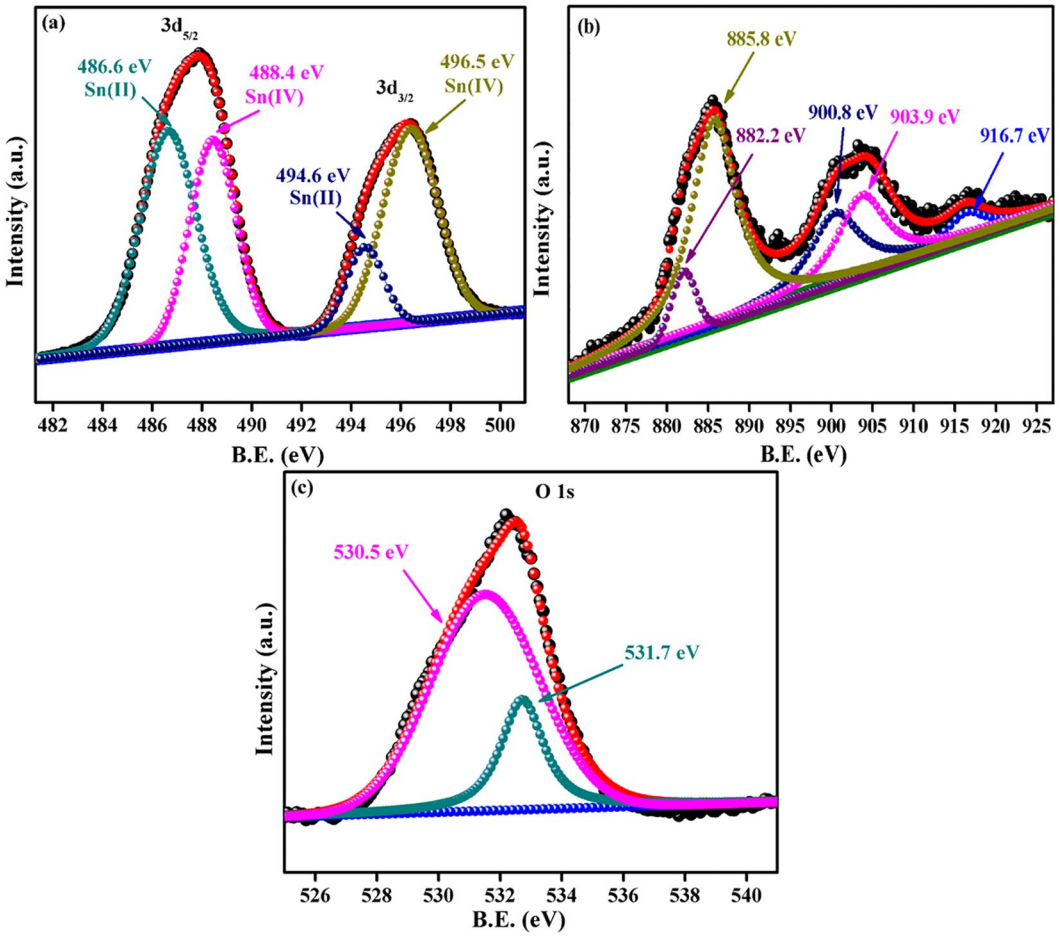

Figure 5. XPS core level spectra of (**a**) Sn 3d (**b**) Ce 3d and (**c**) O 1 s for 9 wt.% Ce doped SnO_2 sample.

respectively. The resistance of sensing materials increased or decreased to the exposure and removal of chemical inputs. The gas sensitivity is defined as follows;

$$S_R = \frac{R_g - R_a}{R_a} \times 100 \quad \text{(For reducing gas)} \tag{1}$$

$$S_O = \frac{R_a - R_g}{R_g} \times 100 \quad \text{(For oxidizing gas)} \tag{2}$$

where, Rg is the electrical resistance in presence of gas and Ra is the electrical resistance in clean synthetic air atmosphere only. Figure 6(a,b) shows the repeatable operation cycles of 9 and 6% Ce doped SnO_2 sensors in the ethanol exposure at RT. The response signal of 9, 6 and 3% Ce doped SnO_2 sensors for various amount of concentration at RT is shown in Fig. 6(a–c). Figure 6(d) shows the response signal of 9% Ce doped SnO_2 sensors for NO_2 and ethanol exposure. It has also been observed that sensor response (recovery) times are of the order of ~5–30 secs (30–60 secs) as seen from Fig. 6(a–d). The sensor response of pure and Ce doped SnO_2 as a function of ethanol concentration is shown in Fig. 7(a). It is evident from the Fig. that 9% Ce doped SnO_2 sensor exhibits higher sensitivity for various amount of ethanol concentration at RT. The 9% Ce doped SnO_2 sensor shows a striking improvement of RT ethanol sensing behaviour as compared to pure SnO_2. Selectivity behaviour of the pure and Ce doped SnO_2 sensor was tested with 400 ppm of C_2H_5OH (ethanol), NH_3 (ammonia) and NO_2 gas.

The sensitivity values for all the above-mentioned chemical inputs are shown in Fig. 7(b). We can clearly observe from the Fig. 7(b) that 9% Ce doped SnO_2 sensor is highly selective to ethanol gas at RT. The use of the sensing device for longer duration with accuracy depends upon reproducibility, reliability and repeatability. The sensor performance should not vary with time and operation cycles. The stability of 9% Ce doped SnO_2 sensor towards ethanol at RT has been studied for 180 days. It has been confirmed that 9% Ce doped SnO_2 sensor displays better stability and repeatability even at the end of 6th month which is ~97–98% as compared to initial measurements (see Supporting Information, Fig. S5). Such stability and repeatability analysis suggest that the 9% Ce doped SnO_2 sensor can be used for long duration, which is one of the major advantages for practical applications.

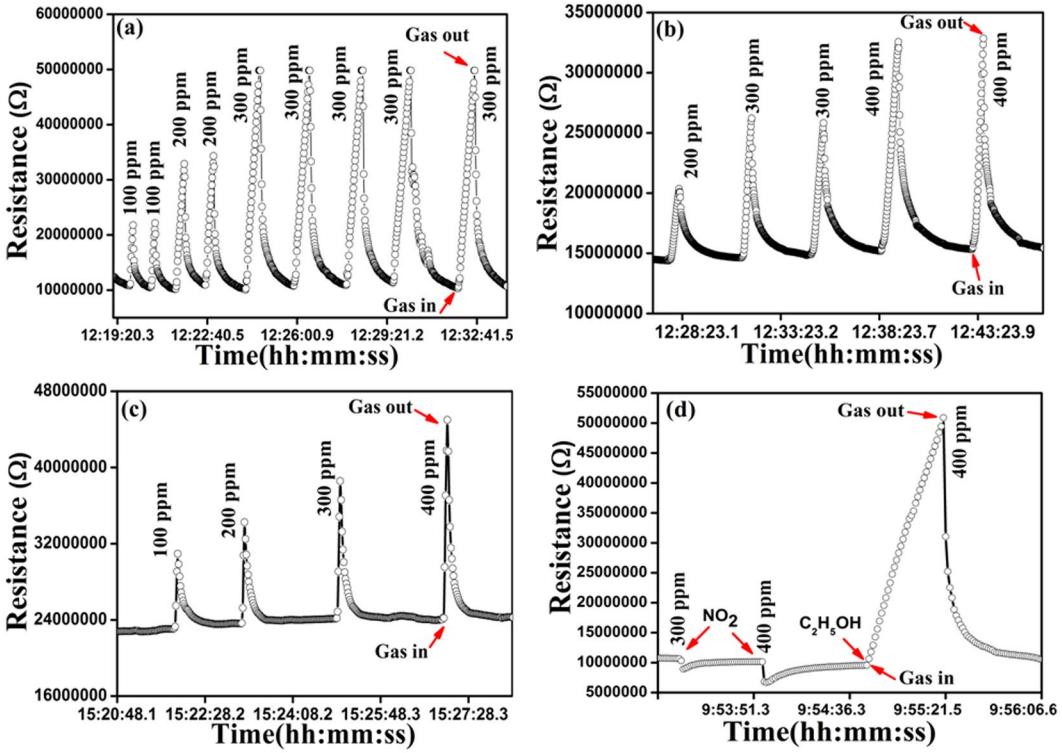

Figure 6. (**a**) Reproducibility of 9% Ce doped SnO_2 sensor response for 200, 300 & 400 ppm of ethanol (**b**) Changes in sensing response exhibited for 200, 300 and 400 ppm of ethanol by 6% Ce doped SnO_2 sensor and (**c**) Response of 3% Ce doped SnO_2 sensor for 100, 200, 300 & 400 ppm of ethanol (**d**) Response of 9% Ce doped SnO_2 sensor for NO_2 and ethanol.

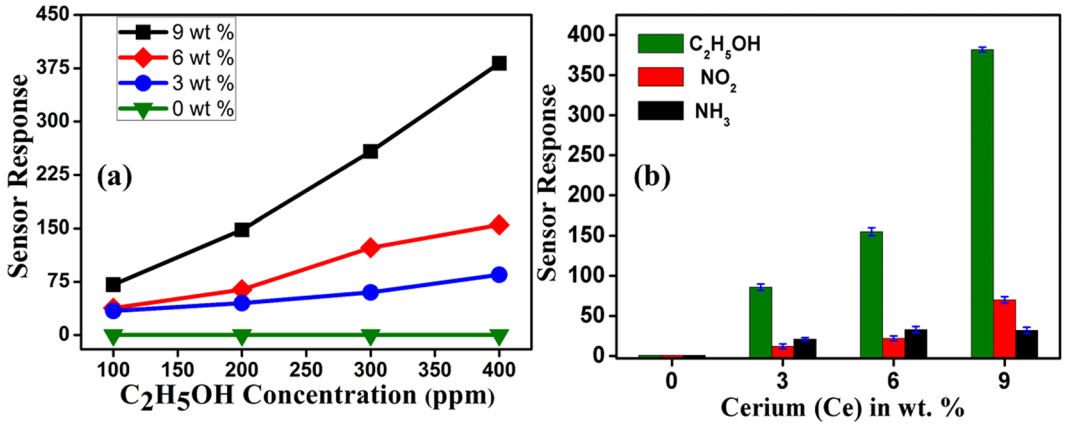

Figure 7. (**a**) Linearity of sensor response shown over concentration of 100, 200, 300 and 400 ppm ethanol for pure SnO_2 and Ce doped SnO_2 sensor (**b**) Sensor response of pure and Ce doped SnO_2 sensor as a function of Ce concentrations at 400 ppm of each C_2H_5OH, NO_2 and NH_3 gas.

Discussion

As it is clear that the undoped SnO_2 will never exhibit p-type semiconducting behaviour. In order to overcome the barriers regarding the enhancement of the gas sensing, different amount of Ce has been doped into pure n-type SnO_2 and sensing measurements of p-type Ce doped SnO_2 has been studied systematically. As shown in Fig. 7(a), a linear sensor response has been observed for $C_2H_5O_5$ concentration (ppm) varying from 100 to 400 ppm indicating enhanced sensing for 9 wt% Ce doped SnO_2 material at RT. As discussed from XRD measurements, it is evident that Ce has been incorporated in SnO_2 lattice which causes increase in lattice parameter and micro strain. From the above analysis, it is confirmed that defect chemistry has been modified with the incorporation of Ce into SnO_2. The assumptions regarding defect states can be made in order to identify the type of defects induced in the structure with doping: (i) substitution of Ce in place of Sn (Ce_{Sn}) (ii) interstitial oxygen (O_i) formation because of the occupation of Sn position by Ce atom and (iii) a complex defect ($Ce_{Sn} + 2O_i$) may be

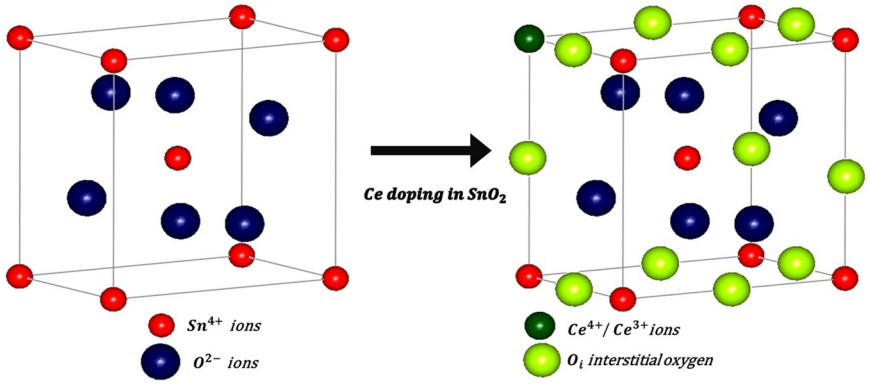

Figure 8. Schematic illustration of effect of Ce doping in SnO_2 lattice.

present at the Sn site. Figure 8 shows the schematic illustration of defect chemistry caused by Ce doping in SnO_2 lattice. In order to justify the drastically enhanced sensing mechanism in Ce doped SnO_2, one needs to identify the dominance of the defects as mentioned above and an in-depth analysis is required. As discussed earlier from the ESR measurements, it is clear that there is a strong exchange of unpaired electrons and delocalized unpaired electrons in the form of free radicals. Small ΔHpp and high intensity is observed in 9% Ce-doped SnO_2 may be attributed to the existence of large number of intrinsic oxygen vacancies. This suggested that the increase in the Ce doping concentrations leads to the increase in the interstitial oxygen atoms present in the structure/system. This is because there is a reduction in the Sn content via substitution of Ce (Ce_{Sn}) which is also evident from EDS analysis (see Supporting Information, Fig. S4). Hence, it is revealed that the doping conditions have been resulted in Sn-poor/O-rich condition which should be the reason for p-type semiconductor[34,60]. From the literature, it is confirmed that the Ce_{Sn} acts as a donor because of the lower formation energy. In addition, the complex defect ($Ce_{Sn} + 2O_i$) present at the Sn site consists of relatively high formation energy and behaves as an acceptor. It is here to be understood that there is a chance of existence of self-compensation between lower formations energized donors and acceptors respectively. Such self-compensation will suppress Ce_{Sn} by ($Ce_{Sn} + 2O_i$) complex defect and can be predicted to behave like an acceptor concluding that the Ce doped SnO_2 behaves as a p-type semiconductor. It has been confirmed that, when C_2H_5OH gas exposed to all the sensors, the 9% Ce-doped SnO_2 sensor shows the highest response (SR = 382) for 100 to 400 ppm concentrations of C_2H_5OH at RT. The improved sensors response of the p-type Ce-doped SnO_2 nanostructures to ethanol at RT can be studied in more detail in order to clarify sensing mechanism. The defect of the p-type Ce-doped SnO_2 and their sensing mechanism can be explained using the following reactions 3, 4 and 5 (in Kröger-Vink notation)[30,61].

$$SnO_2 \rightarrow 2Ce_{Sn} + 3O_0^X + V_0^{\cdot\cdot} \tag{3}$$

$$\frac{1}{2}O_{2(g)} \leftrightarrow O_{(ads)}^- + h^{\cdot} \tag{4}$$

However, Ce_{Sn} is the Ce substitution in Sn sites and O_0^X is the lattice oxygen and $V_0^{\cdot\cdot}$ denotes the two positively charged vacancies on an oxygen sites. Thus, in p-type Ce-doped SnO_2, the adsorption of negatively charged oxygen ion can produce the holes for conduction which is shown in the reaction-4[62]. The interactions between ethanol and surface adsorbed oxygen in p-type Ce-doped SnO_2 can be described by reaction 5. The resulting gas-sensing equation may be considered according to the charges of the adsorbed oxygen ions under the hypothesis of complete oxidation of C_2H_5OH.

$$C_2H_5OH_{(g)} + 6O_{(ads)}^- + 6h^{\cdot} \rightarrow 2CO_{2(g)} + 3H_2O_{(g)} \tag{5}$$

Thus, complete oxidation of C_2H_5OH in the above reactions increased the resistance and concurrently decreases the conductance of the surface region of p-type Ce-doped SnO_2 upon exposure to ethanol. Such changes in resistance while exposure to ethanol in Ce-doped sensors shown in Fig. 6.

In order to summarize the improved gas sensing behaviour of 9 wt % Ce doped SnO_2 sensor towards ethanol at RT, four major factors are responsible (i) more structural defects present in the sample, (ii) particle size becomes twice of the Debye length and (iii) high surface to volume ratio and (iv) presence of a large number of unpaired electrons on the sensor surface. It can therefore, be inferred from XRD analysis that Ce doping in SnO_2 leads to an increase in lattice strain as well as deviation from atomic position of the host material observed. This deviation from atomic position of the host material and increased lattice strain will result in the formation of more structural defects within the system. When Sn is substituted by isovalent Ce atoms, Ce^{4+} could be easily reduced to Ce^{3+} which leads to the formation of an acceptor-like defects resulting the Ce doped SnO_2 behaviour as a p-type semiconductor[30]. On the other hand, it was essential to mention that above 3% Ce, the semiconducting behaviour transforms into p-type which has been one of the reason for the drastic increase in ethanol sensing. Analogous behaviour has been reported by Chattopahhyay and co-workers in case of Al doped SnO_2[63]. It has been reported that below 12.05% Al substitution in SnO_2, the sample exhibited n-type semiconducting

Materials Used	Deposition Technique	Operating temperature	Sensor Response	Response Time (Sec)	Recovery Time (Sec)	Reference
50 vol.% SnO_2-ZnO	Combinational solution	300	4.69	72	NA	[70]
50 wt.% SnO_2-ZnO	Electrospinning	360	17	5	1	[71]
5 wt.% La_2O_3-SnO_2	Powder solution coating	300	740	1200	1200	[72]
$ZnSnO_3$@SnO_2	Hydrothermal	270	27.8	1	1.8	[73]
1.5 mol% Fe_2O_3-SnO_2	Sol-gel	250	24	NA	NA	[74]
ZnO	Solvothermal	320	9.7	35	37.1	[75]
ZnO	Alkaline precipitation	300	275	36	35	[76]
ZnO/SnO_2	Electrospinning	300	23	150	1100	[77]
MoO_3	Exfoliation	300	33	21	10	[78]
In_2O_3/CuO	Sputtering	250	9.6	48	30	[79]
ZnO/SnO_2	Hydrothermal	200	380	74	12	[80]
WO_3	Hydrothermal	200	11.3	8.5	65	[81]
ZnO/SnO_2	Hydrothermal	150	14.7	10	23	[82]
9 wt.% Ce doped SnO_2	Drop casting	*RT*	382	~5–20	~30–60	***This work***

Table 3. Comparison of the ethanol sensing capability of 9 wt% Ce doped SnO_2 sensor in this study to those of the previous reports.

behaviour, and it transforms to p-type above it. Aforementioned XPS results indicated that Ce^{3+} substitution at Sn^{4+} site leads to the formation of an acceptor-like defects in Ce doped SnO_2 sample and introduced the excess amount of holes which in turn increases oxygen vacancies in the lattice[64–67]. Such increase in the defects can contribute well in the direction of achieving improved sensing to ethanol at RT. The highest sensor response noticed in 9 wt.% Ce-doped SnO_2 is associated to increased oxygen vacancies in SnO_2 lattice that provides active sites for adsorption of ethanol gas molecules at RT. Comprehending the statement that enhanced RT sensor response to ethanol in 9 wt.% Ce-doped sensors may result in formation of oxygen vacancies in the host materials. This conclusive statement is in agreement with ESR studies. From ESR studies, it is well-defined that oxygen vacancies are higher in case of 9 wt.% Ce-doped sensors. In addition, power absorption and peak to peak line width during resonance increases remarkably with Ce doping. Small ΔHpp and highest intensity is noticed in 9% Ce doped SnO_2 and resulted into the existence of large number of free electrons in the form of oxygen vacancies. Increase in sensitivity due to higher oxygen vacancies is previously reported in literature[68,69]. FESEM studies also confirmed that 9 wt % Ce doped SnO_2 sensor exhibited the lowest grain size ~8 (2) nm and the number of grain boundaries increases by decreasing the gain size (see Supporting Information, Fig. S3). Therefore, surface areas increase steadily with the increased Ce concentration. Hence 9 wt % Ce doped SnO_2 sensor shows a higher sensor response to ethanol at RT due to their larger surface areas. More surface areas provide more active sites for the adsorption of the chemical inputs which are responsible for the improvement of the gas sensor response. As discussed earlier from the TEM analysis, the variation in the particle size from 16 nm to 6 nm has been observed for the doping wt% ranging from 0 to 9% respectively. To understand the effect of particle size on the sensing mechanism, one needs to establish the relationship of particle size with Debye length depending on the type of metal oxide, the analyzed gas, and detection mechanism to be taken place[28]. The main fundamental parameter to evaluate the gas response is related to the Debye length (LD). There may be three cases to be assumed: (i) $d \gg 2Ls$ (ii) $d \sim 2Ls$ (iii) $d < 2Ls$. From the literature, it is considered that LD of SnO_2 is about ~3 nm. In case of 0%, 3% and 6% Ce-SnO_2, assumption 1 has been satisfied stating that the gas sensitivity may be practically independent of d because of the conduction mechanism taking place across the grain boundary is limited by Schottky barriers. But in case of 9% Ce-SnO_2, the particle size becomes twice of the Debye length i.e. $d \sim 2Ls$. This shows that the conductive channels between grains are overlapped attributed to the complete depletion of space charge region while interacting with the oxygen molecules. Hence, whole particle takes part in the gas sensing and as a result higher sensitivity is observed. So, the major factor for the higher sensing are attributed to the increased concentration of adsorbed oxygen species on the fully depleted junctions across the grains resulting into the higher sensing for ethanol at RT. In Table 3, the ethanol sensing response of the 9 wt% Ce doped SnO_2 sensors are compared with those of the earlier published reports[70–82]. Table 3 displays marterials used, deposition technique, operating temperatures, sensor response, and recovery times of some ethanol sensors. However, sensor response of SnO_2 based sensors are good, but operating temperatures are very high. On the other hand, it must also be observed from the present study that the 9 wt% Ce doped SnO_2 sensor remarkably enhanced the ethanol sensor response at RT with faster response (recovery) time ~5–20 sec (~30–60 sec). Hence, the strikingly improved sensor response of 9% Ce-doped SnO_2 sensor upon exposure of C_2H_5OH is associated to the uniformly distributed nanoparticles with size approximately twice of the Debye length, high surface area, defect chemistry and presence of a large number of unpaired electrons of the sensor surface.

Conclusions

In conclusion, systematic studies have been performed on the synthesis, characterization and RT gas sensing behaviour of p-type Ce doped SnO_2 sensor. Pure and Ce doped SnO_2 sensor have been successfully synthesized by chemical co-precipitation method and used to detect ethanol at RT. To the best of our knowledge, this is the first time a p-type Ce-doped SnO_2 has been studied and demonstrated to meet the requirements for highly sensitive,

selective and long-time stable low cost sensing device. The maximum sensitivity is ~382 for 400 ppm with fast response time of ~5 to 25 sec have been obtained in 9% Ce doped SnO_2 towards ethanol at RT. The high sensitivity of Ce doped SnO_2 sensor towards C_2H_5OH is attributed to the uniformly distributed nanoparticles with size approximately twice of the Debye length, defect chemistry, presence of a large number of unpaired electrons, and creating the excess of holes, as oxygen vacancies. This study suggests a practical approach to the fabrication and design of high performance ethanol sensors working at RT.

Experimental

Materials and Reagents. Tin(IV) chloride pentahydrate ($SnCl_4.5H_2O$), cerium(III) Chloride heptahydrate ($CeCl_3{\cdot}7H_2O$), and stearic acid were purchased from Sigma-Aldrich. Ethanol (C_2H_5OH) and ammonia were purchased from Merck limited. All reagents were used without further purification.

Synthesis. In present work, pure and Ce doped SnO_2 samples are synthesized with three different Ce concentrations (the mole ratio of Ce/Sn = 3, 6 and 9 wt%) through a chemical co-precipitation method. Ethanol is used as a solvent for the synthesis of metal oxide nanoparticles. In a typical synthesis of Ce doped SnO_2 sensor, $SnCl_4.5H_2O$ and $CeCl_3.7H_2O$ in stoichiometric proportions were dissolved in ethanol (C_2H_5OH). For the precipitation of the solution, ammonia and stearic acid was added drop wise to the precursor solution with continuous stirring and the final pH was maintained at 10. Obtained precipitates were filtered and washed several times with absolute alcohol and distilled water, then dried in a vacuum oven at 95 °C for 4 hours. These obtained powder samples (undoped and Ce doped SnO_2) were annealed at 800 °C for six hours using a muffle furnace and were cool down at the rate of 100 °C per hour. The obtained powder samples have been used to fabricate the sensor device. The gold interdigital six finger electrodes patterns were deposited on the alumina substrates by thermal evaporation. The width of each finger is 500 µm and the interspacing between the fingers is 700 µm respectively. Then, the gas sensor was fabricated by drop casting technique. The pure and Ce-doped SnO_2 dispersed in appropriate amount of ethanol followed by ultrsonication for 30 minutes. Thereafter, the solution was drop casted on the Au interdigital electrodes patterned substrate. The deposited sensor films were sintered at 95 °C for 30 minutes in a vacuum oven.

Characterizations. The samples were characterized using X-ray diffraction (XRD, Bruker D8 advanced diffractometer) in the scanning range of 20–80° (2θ) with the step size of 0.0195° using Cu-Kα radiations at 1.54 Å wavelength. The Rietveld refinement of XRD data has been done by FULLPROF program. Surface morphology and chemical composition of sensor materials were determined using field emission scanning electron microscope (FESEM, Model Σigma, Carl Ziess). The morphological and structural information were carried out using high-resolution transmission electron microscope (TEM, FEI Technai G230, Hillsboro, U.S.A.). To study the presence of unpaired electrons, electron spin resonance (ESR) spectra was recorded at RT by using ESR X-band spectrometer operating at 9.45 GHz frequency, 2.99 mW power with the sweeping time of 2 mins. X-ray photoelectron spectroscopy XPS (Perkin Elmer-1257 with hemispherical section analyzer with 25 meV resolution) has been used. XPS set up consist of dual anode X-ray source, which is capable of generating Al Kα (1486.6 eV) or Mg Kα (1253.6 eV) X-ray radiations. The sensing measurements were performed in custom designed gas sensing set up attached with mass flow controllers for precise measurement of gas flow at ppm level[39,83].

References

1. Rout, C. S., Hegde, M., Govindaraj, A. & Rao, C. Ammonia sensors based on metal oxide nanostructures. *Nanotechnology* **18**, 205504 (2007).
2. Quang, N. H., Van Trinh, M., Lee, B.-H. & Huh, J.-S. Effect of NH 3 gas on the electrical properties of single-walled carbon nanotube bundles. *Sensors and Actuators B: Chemical* **113**, 341–346 (2006).
3. Rao, A. *et al. In Situ* Localized Growth of Ordered Metal Oxide Hollow Sphere Array on Microheater Platform for Sensitive, Ultra-Fast Gas Sensing. *ACS Applied Materials & Interfaces* (2017).
4. Franke, M. E., Koplin, T. J. & Simon, U. Metal and metal oxide nanoparticles in chemiresistors: does the nanoscale matter? *Small* **2**, 36–50 (2006).
5. Korotcenkov, G. Metal oxides for solid-state gas sensors: What determines our choice? *Materials Science and Engineering: B* **139**, 1–23 (2007).
6. Yamazoe, N. & Miura, N. Environmental gas sensing. *Sensors and Actuators B: Chemical* **20**, 95–102 (1994).
7. Qu, F., Yuan, Y. & Yang, M. Designed Synthesis of Sn_3N_4 Nanoparticles through Soft Urea Route with Excellent Gas Sensing Properties. *Chemistry of Materials* (2017).
8. Watson, J. The tin oxide gas sensor and its applications. *Sensors and Actuators* **5**, 29–42 (1984).
9. Wang, S., Liu, X. & Zhang, M. Reduction of Ammineruthenium (III) by Sulfide Enables *In Vivo* Electrochemical Monitoring of Free Endogenous Hydrogen Sulfide. *Analytical Chemistry* (2017).
10. Wetchakun, K. *et al.* Semiconducting metal oxides as sensors for environmentally hazardous gases. *Sensors and Actuators B: Chemical* **160**, 580–591 (2011).
11. Zhang, J., Qin, Z., Zeng, D. & Xie, C. Metal-oxide-semiconductor based gas sensors: screening, preparation, and integration. *Physical Chemistry Chemical Physics* **19**, 6313–6329 (2017).
12. Korotcenkov, G., Brinzari, V. & Cho, B. K. Conductometric gas sensors based on metal oxides modified with gold nanoparticles: a review. *Microchimica Acta* **183**, 1033–1054 (2016).
13. Koo, W.-T. *et al.* Heterogeneous Sensitization of Metal–Organic Framework Driven Metal@ Metal Oxide Complex Catalysts on an Oxide Nanofiber Scaffold Toward Superior Gas Sensors. *Journal of the American Chemical Society* **138**, 13431–13437 (2016).
14. Mirzaei, A., Leonardi, S. & Neri, G. Detection of hazardous volatile organic compounds (VOCs) by metal oxide nanostructures-based gas sensors: A review. *Ceramics International* **42**, 15119–15141 (2016).
15. Xu, X., Fan, H., Liu, Y., Wang, L. & Zhang, T. Au-loaded In_2O_3 nanofibers-based ethanol micro gas sensor with low power consumption. *Sensors and Actuators B: Chemical* **160**, 713–719, https://doi.org/10.1016/j.snb.2011.08.053 (2011).
16. Hwang, I.-S. *et al.* Synthesis and gas sensing characteristics of highly crystalline ZnO–SnO_2 core–shell nanowires. *Sensors and Actuators B: Chemical* **148**, 595–600, https://doi.org/10.1016/j.snb.2010.05.052 (2010).

17. Khoang, N. D., Trung, D. D., Van Duy, N., Hoa, N. D. & Van Hieu, N. Design of SnO_2/ZnO hierarchical nanostructures for enhanced ethanol gas-sensing performance. *Sensors and Actuators B: Chemical* **174**, 594–601, https://doi.org/10.1016/j.snb.2012.07.118 (2012).
18. Moon, C. S., Kim, H.-R., Auchterlonie, G., Drennan, J. & Lee, J.-H. Highly sensitive and fast responding CO sensor using SnO_2 nanosheets. *Sensors and Actuators B: Chemical* **131**, 556–564, https://doi.org/10.1016/j.snb.2007.12.040 (2008).
19. Wang, Y., Wu, X., Li, Y. & Zhou, Z. Mesostructured SnO_2 as sensing material for gas sensors. *Solid-State Electronics* **48**, 627–632, https://doi.org/10.1016/j.sse.2003.09.015 (2004).
20. Batzill, M. & Diebold, U. The surface and materials science of tin oxide. *Progress in Surface Science* **79**, 47–154, https://doi.org/10.1016/j.progsurf.2005.09.002 (2005).
21. Pourfayaz, F., Mortazavi, Y., Khodadadi, A. & Ajami, S. Ceria-doped SnO_2 sensor highly selective to ethanol in humid air. *Sensors and Actuators B: Chemical* **130**, 625–629, https://doi.org/10.1016/j.snb.2007.10.018 (2008).
22. Alcántara, R. *et al*. Preparation, sintering, and electrochemical properties of tin dioxide and Al-doped tin dioxides obtained from citrate precursors. *Chemistry of materials* **12**, 3044–3051 (2000).
23. Kılıç, Ç. & Zunger, A. Origins of coexistence of conductivity and transparency in SnO_2. *Physical Review Letters* **88**, 095501 (2002).
24. Aswal, D. K. & Gupta, S. K. *Science and technology of chemiresistor gas sensors*. (Nova Publishers, 2007).
25. Das, S. & Jayaraman, V. SnO_2: A comprehensive review on structures and gas sensors. *Progress in Materials Science* **66**, 112–255, https://doi.org/10.1016/j.pmatsci.2014.06.003 (2014).
26. Akira, F., Taneo, N. & Yoshihiro, H. Hall-Effect Measurement on Polycrystalline SnO $_2$ Thin Films. *Japanese Journal of Applied Physics* **27**, 552 (1988).
27. Pourfayaz, F., Khodadadi, A., Mortazavi, Y. & Mohajerzadeh, S. S. CeO_2 doped SnO_2 sensor selective to ethanol in presence of CO, LPG and CH4. *Sensors and Actuators B: Chemical* **108**, 172–176, https://doi.org/10.1016/j.snb.2004.12.107 (2005).
28. Korotcenkov, G. The role of morphology and crystallographic structure of metal oxides in response of conductometric-type gas sensors. *Materials Science and Engineering: R: Reports* **61**, 1–39, https://doi.org/10.1016/j.mser.2008.02.001 (2008).
29. Wang, Z., Zhou, H., Han, D. & Gu, F. Electron compensation in p-type 3DOM NiO by Sn doping for enhanced formaldehyde sensing performance. *Journal of Materials Chemistry C* **5**, 3254–3263 (2017).
30. Zhang, G., Xie, C., Zhang, S., Zhang, S. & Xiong, Y. Defect chemistry of the metal cation defects in the p-and n-doped SnO2 nanocrystalline films. *The Journal of Physical Chemistry C* **118**, 18097–18109 (2014).
31. Tran, Q.-P., Fang, J.-S. & Chin, T.-S. Optical Properties and Boron Doping-Induced Conduction-Type Change in SnO_2 Thin Films. *Journal of Electronic Materials* **45**, 349 (2016).
32. Varley, J. *et al*. High-throughput design of non-oxide p-type transparent conducting materials: data mining, search strategy and identification of boron phosphide. *Chemistry of Materials* (2017).
33. Wahila, M. J. *et al*. Lone-pair stabilization in transparent amorphous tin oxides: a potential route to p-type conduction pathways. *Chemistry of Materials* **28**, 4706–4713 (2016).
34. Scanlon, D. O. & Watson, G. W. On the possibility of p-type SnO2. *Journal of Materials Chemistry* **22**, 25236–25245, https://doi.org/10.1039/C2JM34352E (2012).
35. Rastomjee, C. S. *et al*. An investigation of doping of SnO_2 by ion implantation and application of ion-implanted films as gas sensors. *Thin Solid Films* **279**, 98–105, https://doi.org/10.1016/0040-6090(95)08156-9 (1996).
36. Qin, W., Xu, L., Song, J., Xing, R. & Song, H. Highly enhanced gas sensing properties of porous SnO_2-CeO_2 composite nanofibers prepared by electrospinning. *Sensors and Actuators B: Chemical* **185**, 231–237, https://doi.org/10.1016/j.snb.2013.05.001 (2013).
37. McCarthy, G. J. & Welton, J. M. X-ray diffraction data for SnO_2. *An illustration of the new powder data evaluation methods. Powder Diffraction* **4**, 156–159 (1989).
38. Rüdorff, W. & Valet, G. Über das Ceruranblau und Mischkristalle im System $CeO_2 \cdot UO_2 \cdot U_3O_8$. *Zeitschrift für anorganische und allgemeine Chemie* **271**, 257–272 (1953).
39. Kumar, M., Kumar, A. & Abhyankar, A. Influence of texture coefficient on surface morphology and sensing properties of w-doped nanocrystalline tin oxide thin films. *ACS applied materials & interfaces* **7**, 3571–3580 (2015).
40. Lou, X. *et al*. Epitaxial Growth of Mg $\times$ $Ca_{1\times x}$ O on GaN by Atomic Layer Deposition. *Nano letters* **16**, 7650–7654 (2016).
41. Jiang, Z. *et al*. Highly sensitive and selective butanone sensors based on cerium-doped SnO_2 thin films. *Sensors and Actuators B: Chemical* **145**, 667–673 (2010).
42. Yang, L. *et al*. Efficient hydrogen evolution over Sb doped SnO_2 photocatalyst sensitized by Eosin Y under visible light irradiation. *Nano Energy* (2017).
43. Cullity, B. Element of X-ray Diffraction, Addison-Wesley Reading. *MA Google Scholar* (1978).
44. Shi, S., Gao, D., Xu, Q., Yang, Z. & Xue, D. Singly-charged oxygen vacancy-induced ferromagnetism in mechanically milled SnO2 powders. *RSC Advances* **4**, 45467–45472, https://doi.org/10.1039/C4RA05475J (2014).
45. Irzh, A., Genish, I., Klein, L., Solovyov, L. A. & Gedanken, A. Synthesis of ZnO and Zn nanoparticles in microwave plasma and their deposition on glass slides. *Langmuir* **26**, 5976–5984 (2010).
46. Volodin, A. & Cherkashin, A. ESR spectra of O_{2-} on SnO_2. effect of adsorbed CO on the conditions of stabilization of O_{2-}. *Reaction Kinetics and Catalysis Letters* **17**, 323–327 (1981).
47. Grutsch, P., Zeller, M. & Fehlner, T. Electronic energies of tin compound. *Inorganic Chemistry* **12**, 1432 (1973).
48. Stranick, M. A. & Moskwa, A. SnO by XPS. *Surface Science Spectra* **2**, 45–49 (1993).
49. Ansari, S., Fouad, H., Shin, H.-S. & Ansari, Z. Electrochemical enzyme-less urea sensor based on nano-tin oxide synthesized by hydrothermal technique. *Chemico-biological interactions* **242**, 45–49 (2015).
50. Zhang, S., Kang, P. & Meyer, T. J. Nanostructured tin catalysts for selective electrochemical reduction of carbon dioxide to formate. *Journal of the American Chemical Society* **136**, 1734–1737 (2014).
51. Nefedov, V., Gati, D., Dzhurinskii, B., Sergushin, N. & Salyn, Y. V. X-ray electron study of oxides of elements. *Zhurnal Neorganicheskoi Khimii* **20**, 2307–2314 (1975).
52. Paparazzo, E., Ingo, G. & Zacchetti, N. X-ray induced reduction effects at CeO_2 surfaces: An x-ray photoelectron spectroscopy study. *Journal of Vacuum Science & Technology A: Vacuum, Surfaces, and Films* **9**, 1416–1420 (1991).
53. Dauscher, A. *et al*. Characterization by XPS and XAS of supported $Pt/TiO_2 \cdot CeO_2$ catalysts. *Surface and Interface Analysis* **16**, 341–346 (1990).
54. Praline, G., Koel, B., Hance, R., Lee, H.-I. & White, J. X-ray photoelectron study of the reaction of oxygen with cerium. *Journal of Electron Spectroscopy and Related Phenomena* **21**, 17–30 (1980).
55. Ingo, G., Paparazzo, E., Bagnarelli, O. & Zacchetti, N. XPS studies on cerium, zirconium and yttrium valence states in plasma-sprayed coatings. *Surface and Interface Analysis* **16**, 515–519 (1990).
56. Supothina, S. & De Guire, M. R. Characterization of SnO_2 thin films grown from aqueous solutions. *Thin Solid Films* **371**, 1–9 (2000).
57. Kumar, V. *et al*. The role of surface and deep-level defects on the emission of tin oxide quantum dots. *Nanotechnology* **25**, 135701 (2014).
58. Chen, M. *et al*. X-ray photoelectron spectroscopy and auger electron spectroscopy studies of Al-doped ZnO films. *Applied Surface Science* **158**, 134–140 (2000).
59. Lee, S. *et al*. Oxygen partial pressure dependent electrical conductivity type conversion of phosphorus-doped ZnO thin films. *Journal of Physics D: Applied Physics* **47**, 065306 (2014).

60. Godinho, K. G., Walsh, A. & Watson, G. W. Energetic and Electronic Structure Analysis of Intrinsic Defects in SnO_2. *The Journal of Physical Chemistry C* **113**, 439–448, https://doi.org/10.1021/jp807753t (2009).
61. Jyh Ming, W. A room temperature ethanol sensor made from p-type Sb-doped SnO_2 nanowires. *Nanotechnology* **21**, 235501 (2010).
62. Choi, K.-I. *et al*. C_2H_5OH sensing characteristics of various Co_3O_4 nanostructures prepared by solvothermal reaction. *Sensors and Actuators B: Chemical* **146**, 183–189 (2010).
63. Ahmed, S. F., Khan, S., Ghosh, P. K., Mitra, M. K. & Chattopadhyay, K. K. Effect of Al doping on the conductivity type inversion and electro-optical properties of SnO_2 thin films synthesized by sol-gel technique. *Journal of Sol-Gel Science and Technology* **39**, 241–247, https://doi.org/10.1007/s10971-006-7808-x (2006).
64. Kar, A. & Patra, A. Optical and Electrical Properties of Eu^{3+}-Doped SnO_2 Nanocrystals. *The Journal of Physical Chemistry C* **113**, 4375–4380, https://doi.org/10.1021/jp810777f (2009).
65. Wei, W., Dai, Y. & Huang, B. Role of Cu Doping in SnO_2 Sensing Properties Toward H_2S. *The Journal of Physical Chemistry C* **115**, 18597–18602, https://doi.org/10.1021/jp204170j (2011).
66. Liu, X., Iqbal, J., Wu, Z., He, B. & Yu, R. Structure and Room-Temperature Ferromagnetism of Zn-Doped SnO2 Nanorods Prepared by Solvothermal Method. *The Journal of Physical Chemistry C* **114**, 4790–4796, https://doi.org/10.1021/jp909178x (2010).
67. Tianshu, Z., Hing, P., Li, Y. & Jiancheng, Z. Selective detection of ethanol vapor and hydrogen using Cd-doped SnO_2-based sensors. *Sensors and Actuators B: Chemical* **60**, 208–215, https://doi.org/10.1016/S0925-4005(99)00272-5 (1999).
68. Ge, Y. *et al*. Highly sensitive and rapid chemiresistive sensor towards trace nitro-explosive vapors based on oxygen vacancy-rich and defective crystallized In-doped ZnO. *Sensors and Actuators B: Chemical* **244**, 983–991 (2017).
69. Šutka, A. & Gross, K. A. Spinel ferrite oxide semiconductor gas sensors. *Sensors and Actuators B: Chemical* **222**, 95–105 (2016).
70. Kim, K.-W. *et al*. The selective detection of C_2H_5OH using SnO_2–ZnO thin film gas sensors prepared by combinatorial solution deposition. *Sensors and Actuators B: Chemical* **123**, 318–324 (2007).
71. Khorami, H. A., Keyanpour-Rad, M. & Vaezi, M. R. Synthesis of SnO_2/ZnO composite nanofibers by electrospinning method and study of its ethanol sensing properties. *Applied Surface Science* **257**, 7988–7992 (2011).
72. Jinkawa, T., Sakai, G., Tamaki, J., Miura, N. & Yamazoe, N. Relationship between ethanol gas sensitivity and surface catalytic property of tin oxide sensors modified with acidic or basic oxides. *Journal of Molecular Catalysis A: Chemical* **155**, 193–200 (2000).
73. Yi, Z., Bing, Y.-f, Chang, L., Zheng, W.-t & Zou, G.-t Self-assembly of hierarchical $ZnSnO_3$-SnO_2 nanoflakes and their gas sensing properties. *Transactions of Nonferrous Metals Society of China* **22**, 2451–2458 (2012).
74. Rumyantseva, M. *et al*. Nanocomposites SnO_2/Fe_2O_3: sensor and catalytic properties. *Sensors and Actuators B: Chemical* **118**, 208–214 (2006).
75. Chen, X. *et al*. Self-assembly of ZnO nanoparticles into hollow microspheres via a facile solvothermal route and their application as gas sensor. *CrystEngComm* **15**, 7243–7249 (2013).
76. Ge, L. *et al*. Trisodium citrate assisted synthesis of ZnO hollow spheres via a facile precipitation route and their application as gas sensor. *Journal of Materials Chemistry* **21**, 10750–10754 (2011).
77. Nikan, E., Khodadadi, A. A. & Mortazavi, Y. Highly enhanced response and selectivity of electrospun ZnO-doped SnO_2 sensors to ethanol and CO in presence of CH_4. *Sensors and Actuators B: Chemical* **184**, 196–204 (2013).
78. Ji, F. *et al*. 2D-MoO_3 nanosheets for superior gas sensors. *Nanoscale* **8**, 8696–8703 (2016).
79. Zhang, P.-P., Zhang, H. & Sun, X.-H. A uniform porous multilayer-junction thin film for enhanced gas-sensing performance. *Nanoscale* **8**, 1430–1436 (2016).
80. Li, W. *et al*. Enhanced ethanol sensing performance of hollow ZnO–SnO_2 core–shell nanofibers. *Sensors and Actuators B: Chemical* **211**, 392–402 (2015).
81. Liu, T. *et al*. Porous tungsten trioxide nanolamellae with uniform structures for high-performance ethanol sensing. *CrystEngComm* **18**, 8411–8418 (2016).
82. Ma, X., Song, H. & Guan, C. Enhanced ethanol sensing properties of ZnO-doped porous SnO_2 hollow nanospheres. *Sensors and Actuators B: Chemical* **188**, 193–199 (2013).
83. Kumar, M., Kumar, A. & Abhyankar, A. SnO_2 based sensors with improved sensitivity and response-recovery time. *Ceramics International* **40**, 8411–8418 (2014).

Acknowledgements

This research was supported by the Post-Doctoral Research Program through Incheon National University (INU), Incheon, Republic of Korea and Basic Science Research Program through the National Research Foundation (NRF) of Korea by the Ministry of Education (NRF-2016R1C1B1012088).

Author Contributions

M.K. performed the experiments and wrote the manuscript. V.B. interpreted the data. J.H.Y. and A.C.A. designed the experiments and supervised the project. S.H.P. helped in XPS measurements of the samples. A.K. and J.K. polished the paper.

Additional Information

Supplementary information accompanies this paper at https://doi.org/10.1038/s41598-018-26504-3.

Competing Interests: The authors declare no competing interests.

Publisher's note: Springer Nature remains neutral with regard to jurisdictional claims in published maps and institutional affiliations.